Ecological Indicators 162 (2024) 112024

Contents lists available at ScienceDirect

Ecological Indicators

journal homepage: www.elsevier.com/locate/ecolind

Nonlinear relations of urban morphology to thermal anomalies: A cross-time comparative study based on Grad-CAM and SHAP

Jingxuan Hu [a], Tianhui Fan [b], Xiaolan Tang [a,c], Zhijie Yang [a], Yujie Ren [a,*]

[a] College of Landscape Architecture, Nanjing Forestry University, Nanjing, 210037, China
[b] International Institute for Carbon-Neutral Energy Research, Kyushu University, Fukuoka, 8190395, Japan
[c] Academy of Chinese Ecological Progress and Forestry Studies, Nanjing, 210037, China

ARTICLE INFO

Keywords:
Urban morphology
Thermal anomalies
Interpretable machine learning
Nonlinear relationship

ABSTRACT

Urban thermal anomalies profoundly impact human society, affecting daily life, public health, and residential comfort. Prior studies linked thermal anomalies to urban morphology evolution and land use change during urbanization based on multi-indicator quantification of urban morphology and linear regression modeling. However, it remained unclear which urban morphology elements predominantly dominate thermal anomalies and whether their impact is solely linear, and understanding on the diverse mechanisms through how urban morphology influences various thermal anomalies across seasons remains limited. Therefore, this study employed convolutional neural networks and interpretable machine learning (Grad-CAM and SHAP) to explore nonlinear relationships between urban morphology and thermal anomalies, focusing on comparisons between different types of anomaly events across time. The main findings indicated: (1) Grad-CAM's identification of pivotal hotspot pixels and SHAP's interpretability assessment highlighted that crucial urban morphology factors contributing to thermal anomalies include the area of green spaces, water spaces, the number of residential facilities, building floor area ratio, and the count of industrial production facilities. (2) Clear nonlinear relationships were observed between dominant urban morphology factors and the occurrence of thermal anomalies, which confirming the existence of multiple thresholds and activation levels, as demonstrated through SHAP's partial dependency analysis. The dynamic complexity of these associations significantly varied depending on the type of event and the timing of thermal anomalies. These findings offer actionable guidance for urban planners to refine climate-friendly strategies, revealing the heterogeneity of these relationships across time and seasons through multi-scenario analysis and providing tailored insights for climate-sensitive urban planning.

1. Introduction

With the rapid pace of urbanization, the Earth's surface is increasingly displaying pronounced non-homogeneous characteristics, resulting in significant disparities in thermal environments across various regions. Thermal anomalies in urban areas stand out as tangible evidence of such phenomena. Urban thermal anomalies denote conspicuous temperature variations observed within specific city zones in contrast to their surrounding areas (Twardosz and Kossowska-Cezak, 2021). These variances, often depicted as urban heat or cold islands (Rizwan et al., 2008; Zhang et al., 2015), wield substantial direct and indirect repercussions on human existence, impacting daily routines (Emmanuel and Fernando, 2007), public health (Li et al., 2016), and residential comfort (Sharma et al., 2021). Severe anomalies can precipitate heat stress (Kovats and Hajat, 2008), particularly affecting vulnerable demographics such as the elderly, children, and individuals with chronic ailments (Eugenio Pappalardo et al., 2023; Qiang et al., 2023; Oliveira et al., 2022). Moreover, these anomalies often worsen social inequalities, disproportionately impacting low-income areas due to the lack of water bodies, green spaces, and trees that help regulate temperatures (Ghosh and Das, 2018; Loughner et al., 2012). Understanding these urban thermal anomalies is crucial for grasping urban climates, enhancing environmental quality, improving living conditions, and devising strategies to tackle climate change (Hu and Li, 2020).

Previous research has firmly established the correlation between urban thermal anomalies and the evolution of urban structures in the context of urbanization, coupled with shifts in land use patterns. These research endeavors have extensively explored the linear correlations

* Corresponding author.
E-mail address: renyujie@njfu.edu.cn (Y. Ren).

https://doi.org/10.1016/j.ecolind.2024.112024
Received 15 January 2024; Received in revised form 3 April 2024; Accepted 11 April 2024

between urban thermal anomalies and various urban morphological factors, utilizing meticulously constructed econometric models (Stone and Rodgers, 2001; Yin et al., 2018; Hathway and Sharples, 2012). These factors encompass two-dimensional and three-dimensional architectural configurations, surface biophysical parameters, urban landscape composition, and socioeconomic indicators (Liang, 2021; Liu et al., 2021; Liu et al., 2022; Sanagar Darbani et al., 2021; Schwarz and Manceur, 2015; Zhou et al., 2017). In summary, the theoretical insights gleaned from these studies underscore the critical importance of managing urban morphology as a fundamental approach to mitigating urban thermal anomalies (Steeneveld et al., 2011; Watkins et al., 2023; Kang et al., 2022; Peng et al., 2022; Chen et al., 2024). The configuration of urban functional spaces, architectural design, and the distribution of diverse infrastructural components have been identified as pivotal factors influencing the occurrence of thermal anomalies (Boukhabla et al., 2013; Fitria et al., 2019; Liu and Morawska, 2020; Meng et al., 2022). However, due to the inherent constraints of conventional econometric models, the examination of their interrelations in these studies has predominantly remained confined to linear relationships (Zhao and Du, 2016; O'Shea and Nash, 2023; Parsa, 2020; Selvaraju et al). Indeed, recent experimental research has highlighted variations in the mechanisms through which certain urban morphology features, such as green spaces, impact ecological indicators like air pollutant concentrations, across different scales. These correlation mechanisms exhibit potential non-linear characteristics (Xing, 2020; Abitbol and Karsai, 2020). In exploring non-linear relationships, machine learning models, particularly XGBoost models, have demonstrated significant efficacy and are extensively employed in environmental and ecological research. These models facilitate real-time reporting of the non-linear relationship of any variable within the model by tracking the distribution of model predictions with the training data.

Hence, by synthesizing insights from the literature review alongside recent advancements in the field, this study aims to introduce a machine learning model for identifying key urban morphological indicators influencing urban thermal anomalies, and also intends to explore their nonlinear influence mechanisms. Our primary focus lies in addressing two key research inquiries pertaining to the correlation between urban structure and thermal anomalies: (1) Identification of urban morphology factors influencing thermal anomalies across diverse time spans and seasons.; (2) Exploration of the nonlinear relationships between urban morphological factors and thermal anomalies across varying time spans and seasons. By delving into these inquiries, we aim to shed light on the intricate dynamics shaping urban thermal environments. To achieve these objectives, this study proposed a novel method utilizing remote sensing imagery, convolutional neural networks (CNNs), and interpretable machine learning techniques. Remote sensing imagery provided detailed urban information for thorough urban morphology analysis (Zhao and Du, 2016). CNNs efficiently captured the intricate relationship between urban morphology and thermal anomalies, considering nonlinearities and spatial correlations (O'Shea and Nash, 2023). Incorporating interpretable machine learning methods like SHAP and Grad-CAM (Parsa, 2020; Selvaraju et al) helped interpret the model's predictions, enabling a deeper understanding of the nonlinear relations between urban morphology and thermal anomalies, including nonlinear patterns and threshold effects. These methodologies show promise in examining urban spatial evolution, changes in spatial usage concerning population patterns (Xing, 2020), and socioeconomic levels (Abitbol and Karsai, 2020).

In essence, this study trained a CNN model to classify remote sensing imagery slices and simulate urban thermal anomalies. Afterwards, Grad-CAM was utilized to identify the key urban morphology features linked to these anomalies, clarifying the model's focus points. Finally, the XGBoost model underwent additional training and visualization using SHAP, aiming to explain the nonlinear connection-focusing on nonlinear patterns, activation levels, and threshold effects-between urban morphology and thermal anomalies across different time scenarios. The elucidation of the nonlinear relationship between urban morphology and thermal anomalies in this study not only enhances theoretical understanding in the realms of urban planning and thermal environment, but also furnishes a quantitative foundation for the formulation of sustainable urban planning strategies aimed at mitigating thermal anomalies. Specifically, by delineating the various types, thresholds, and activation levels of key urban morphology indicators that exhibit correlation with urban thermal anomalies, this research facilitates the designation of precise urban morphology benchmarks conducive to effective mitigation efforts.

2. Materials and methods

2.1. Experimental setup and study area

In the specific experimental procedure, this study was primarily structured into four steps (Fig. 1).

Step 1: Remote sensing imagery data preprocessing. The foundational dataset underwent meticulous curation procedures, involving the acquisition, cropping, and classification of raw urban remote sensing images containing thermal anomaly information. The designated locale for the collection site was the central region of Nanjing in Jiangsu Province, China, spanning coordinates from 118°31′36″ E, 32°16′44″ N to 118°55′42″ E, 31°51′15″ N. After image acquisition, a segmentation process was implemented, yielding slices with varying widths of 250 m, 300 m, 500 m, 750 m, and 1500 m, in line with methodologies employed in prior studies utilizing remotely sensed map slices as primary data sources (Xing, 2020; Abitbol and Karsai, 2020). Systematic annotation of these segmented slices followed, encompassing observed annual average land surface temperatures and the identification of thermal anomalies, including both cold and heat islands, throughout the year 2018. The resultant annotated dataset, comprising remote sensing image slices, served as the foundational training data for a Convolutional Neural Network (CNN)-based image classifier model. Detailed data labeling schemes adopted during this process are elucidated in Section 2.2.1 for comprehensive understanding.

Step 2: Thermal anomalies simulation. After completing the data preparation phase, a fine-grained image classifier model utilizing the ResNet-18 architecture was trained to simulate urban thermal anomalies in Nanjing during the year 2018. To validate the efficacy of the model, this study opted for Shanghai as a comparative locale due to its similarity in climate and socio-economic characteristics with Nanjing. Notably, both cities experience a subtropical monsoon climate characterized by concurrent periods of heat and rainfall, and exhibit analogous temperature and humidity trends. Furthermore, they serve as pivotal regional political and economic centers, exerting significant influence within their respective regions. The rapid urban expansion experienced by both cities has engendered comparable challenges commonly associated with metropolitan areas of considerable scale. This congruence in climate and socio-economic factors offers a consistent backdrop for the validation of the model. Remote sensing image slices covering the central urban region of Shanghai (121°22′12″ E, 31°18′8″ N to 121°45′19″ E, 30°52′26″ N) were employed, alongside data pertaining to the annual average land surface temperatures and thermal anomalies observed in 2018. This compilation yielded a comprehensive test dataset essential for evaluating the accuracy of the developed model.

Step 3: Identification of morphology factors related to thermal anomalies. Afterwards, the Grad-CAM was utilized to scrutinize the fundamental mechanisms of the constructed urban thermal anomalies image classifier and to pinpoint urban morphological factors associated with these anomalies. Applying back-propagation to trained weight matrices onto parameter layers enabled the visualization and derivation of gradient matrices that matched the output feature layer dimensions. Weighted vectors for feature layer channels were produced via global spatial average pooling, resulting in heatmaps known as category activation maps. Furthermore, the study quantitatively examined

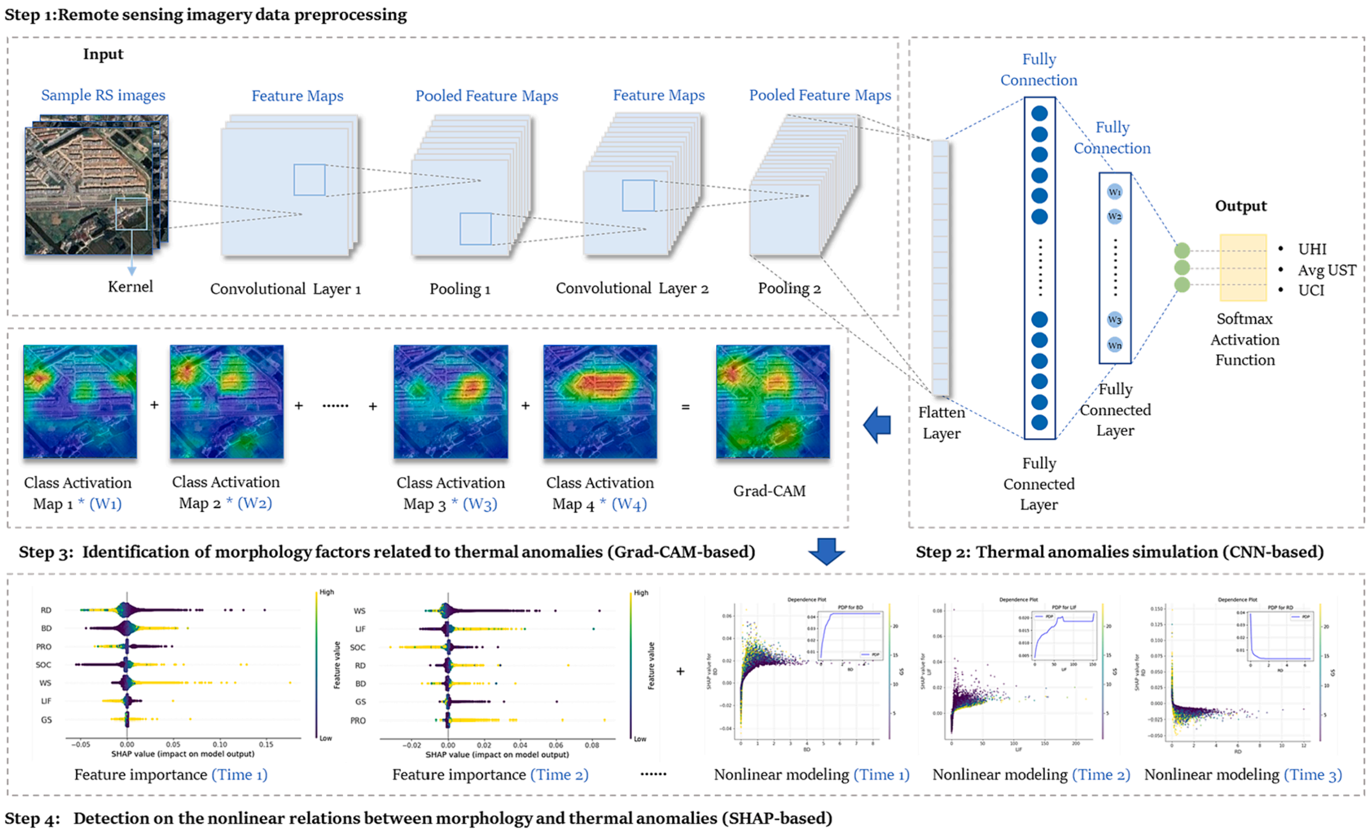

Fig. 1. Research Framework.

correlations between feature values in heatmap pixel areas and urban morphology, revealing spatial connections between urban morphology and thermal anomalies.

Step 4: Detection of the nonlinear relations between morphology and thermal anomalies. The XGBoost model underwent additional training and visualization utilizing SHAP to elucidate the non-linear relationships between urban structure and thermal anomalies across diverse temporal scenarios. Specifically, the XGBoost regression model was constructed with Grad-CAM heat values derived from the thermal anomalies simulation model at resampled pixel locations as the dependent variable, while urban morphology factors served as the independent variables. Moreover, the application of SHAP facilitated a visual examination of the non-linear regression process, accentuating nonlinear patterns, activation levels, and threshold effects.

2.2. Data sources and preprocessing

2.2.1. Urban thermal anomalies dataset

The thermal anomalies data (Fig. 2) utilized in this study were primarily sourced from the Yale Center for Earth Observation (Version 5) (Chakraborty and Lee, 2019). This dataset covered annual, summer, and winter surface urban heat island (SUHI) and surface urban cold island

Fig. 2. Study area and sample of datasets.

(SUCI) intensities data for over 10,000 major cities worldwide. It was compiled using MODIS 8TERRA and AQUA Land Surface Temperature (LST) products, the LANDSCAN urban extent database, 2010 GLOBAL multi-resolution terrain elevation data, and European Space Agency (ESA) Climate Change Initiative (CCI) land cover datasets, employing a simplified urban extent algorithm ("Global Surface UHI Explorer | Center for Earth Observation, 2023).

Specifically, this product provided mean intensity data for urban cluster thermal anomaly events at a pixel level between 2003 and 2018, downscaled to a resolution of 300 m. Distribution and intensity data for urban cold islands and urban heat islands were extracted for Nanjing and Shanghai in 2018 from the subsets "Summer_UHI_yearly_pixel_2018″ and ″Winter_UHI_yearly_pixel_2018″ respectively. The data retrieval process involved the utilization of the Google Earth Engine platform to obtain original ".tiff" format data at a 300-meter resolution. The raw data used in this study, which illustrate the spatial distribution of the thermal environment in Nanjing and Shanghai, are provided in detail in Appendix 1.

2.2.2. XYZ tiles remote sensing imagery dataset

The urban remote sensing imagery data (Fig. 2) utilized in this study were primarily sourced from Gaode Maps' XYZ tiles (Huang, 2019). These map image tiles, acquired via the XYZ protocol, predominantly featured RGB three-band formats such as PNG, diverging from conventional remote sensing images that typically encompass multiple bands (Mete and Yomralioglu, 2021). Traditional remote sensing satellites were equipped with sensors capturing information across diverse bands (Zhu, 2017), facilitating the extraction of comprehensive surface information across various domains (Zurowietz et al., 2018). In contrast, XYZ protocol-based tiled remote sensing images typically comprised standard visible light bands, offering fundamental geographic information and map visualization with a high degree of accessibility (Benhammou, et al., 2022). Within the scope defined in Section 2.1, we gathered 3-meter precision PNG format remote sensing images encompassing central Nanjing and Shanghai from Gaode Maps' XYZ tiles. The acquisition of these images was executed utilizing the XYZ tiles tool embedded in QGIS. To prepare the dataset for simulation models targeting thermal anomalies, the images were systematically cropped into various widths. During the segmentation process of remotely sensed maps in XYZ tile format, we drew upon insights from previous studies involving image manipulation and analysis (Xing, 2020; Abitbol and Karsai, 2020). It is widely observed within the urban study field domain that resizing images to dimensions ranging from 200 to 2,000 m yields optimal results. Notably, varying image dimensions exhibit distinct performance characteristics across different scales. Consequently, we opted to segment the remote sensing images into five specific sizes: 250 m, 300 m, 500 m, 750 m, and 1500 m, resulting in a total of 60,450 slices. These slices underwent annotation, classifying them into 9 distinct labels based on the average annual surface temperatures of 2018 and the occurrence of thermal anomalies. The assigned labels include "No thermal anomaly (AVG)," "Summer daytime heat island (SDUHI)," "Summer nighttime heat island (SNUHI)," "Summer daytime cold island (SDUCI)," "Summer nighttime cold island (SNUCI)," "Winter daytime heat island (WDUHI)," "Winter nighttime heat island (WNUHI)," "Winter daytime cold island (WDUCI)," and "Winter nighttime cold island (WNUCI)."

2.2.3. Urban morphology dataset

The urban morphology data (Fig. 2) utilized in this study were primarily sourced from the OpenStreetMap platform. OpenStreetMap (OSM) stood as an open-source Geographic Information System (GIS) project that furnished global-scale geographic data represented in geofactor forms such as points, lines, and polygons. The platform's geographic dataset encompassed diverse features, including but not limited to roads, buildings, water bodies, subway lines, forests, mountains, shops, restaurants, among others (Vargas-Munoz et al., 2021). The raw data used in this study, which illustrate the spatial distribution of the urban morphology in Nanjing, are provided in detail in Appendix 1.

In the specific context of this study, we predominantly obtained vector graphical data of green spaces, water bodies, main urban roads, secondary urban roads, assorted buildings, social service facilities (hospitals, schools, libraries, community centers, etc.), production facilities (factories, warehouses, farmlands, ports, etc.), and amenities for daily life (shopping centers, entertainment venues, sports facilities, etc.) within the main urban area of Nanjing city (detailed scope outlined in Section 2.1). These datasets aimed to reflect the urban morphology of Nanjing's main urban area.

It's pertinent to note that in subsequent stages of this study (detailed outlined in Section 3.2.2), we quantified the urban green spaces area (GS), water space area (WS), building floor area ratio (BD), road density (RD), as well as the number of social welfare facilities (SOC), industrial production facilities (PRO), and living and residential facilities (LIF) across different grid areas, as per research requirements. The transformation involved converting vectorized graphical data into structured numerical data to facilitate further interpretable machine learning modelling analysis. The rationale behind selecting the quantitative characteristics of the aforementioned urban morphology indicators stems from two key considerations. Firstly, these indicators were pinpointed in our study as being associated with urban thermal anomalies through a Grad-CAM-based computer vision analysis. Secondly, they are commonly recognized as core influencing factors within the literature of related fields.

2.3. Machine learning algorithms

2.3.1. ResNet-18 and transfer learning-based fine-grained image categorization

In this study, a fine-grained image classifier model was built using the pretrained ResNet-18 model (Targ et al., 2023). And transfer learning was leveraged to simulate the occurrences of thermal anomalies in urban remote sensing image slices, including their daily/seasonal variations (Fig. 3). Fine-grained image classification, a computer vision task, aimed to categorize images into highly similar subcategories or subclasses. Unlike conventional image classification tasks, fine-grained classification required differentiating and identifying images belonging to the same category but showing subtle differences (Qi et al., 2019). Fine-grained classification typically involved high similarity among classes, where images from different categories displayed highly similar visual features. Differences usually lay in minute details, covering a large number of categories—often reaching several hundred or even thousands—and encountering limited sample sizes. Due to the restricted number of samples within each subclass, datasets often suffered from imbalances, further complicating the task (Yang et al., 2018).

The specific procedure for constructing the model involved several key steps. Firstly, a dataset of remote sensing image slices was compiled based on identifying thermal anomaly events in 2018, daily/seasonal variations, and associated urban regions. This dataset consisted of fine-grained categories with 9 labels. The Nanjing central area was partitioned to create a training set (48,361 samples) and a validation set (12,089 samples) in an 80 %:20 % ratio, while remote sensing image slices from the central area of Shanghai were assigned as the test set. Secondly, the images were standardized to a uniform size, and data augmentation techniques were applied to expand the dataset and strengthen the model's resilience, aligning with ResNet-18′s input specifications. After these preparations, the pre-trained ResNet-18 model was loaded. The fully connected layer was adjusted to fit the categories in the current dataset, initiating transfer learning. Three distinct approaches were explored during transfer learning: selectively fine-tuning the parameters of the last fully connected layer while keeping other layers fixed, fine-tuning all layers, and initializing all model weights randomly, training all layers from the start. These approaches aimed to optimize the performance of the fine-grained image classifier model for local optima. After undergoing transfer learning and

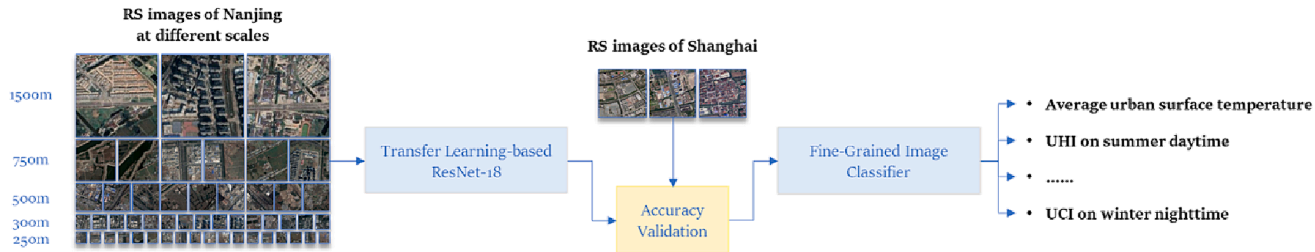

Fig. 3. Procedure of transfer learning-based ResNet-18 Fine-Grained image classifier construction.

achieving optimal model performance, an evaluation of its effectiveness was conducted on the fine-grained classification task, utilizing the validation set prepared during the initial stages of image data preparation, with an 80 %:20 % split ratio (20 % allocated for validation). In addition to utilizing Nanjing data for training and validation purposes, this study augmented its dataset by incorporating thermal anomaly data from Shanghai's downtown area. Given Shanghai's climatic, economic, and geographic similarities to Nanjing, it provided an ideal supplementary locale for constructing a test set. This expansion enabled further simulation and evaluation of the optimized model's performance, with metrics such as validation and testing accuracy being computed (detailed outlined in Section 3.1). The model operates by analyzing remote sensing image slices to classify the presence of urban heat islands or cold islands within a designated area. Furthermore, it forecasts the occurrence time (day or night) and season (summer or winter) of these phenomena.

All model training processes utilized cloud GPU resources (implemented using the PyTorch framework in Python 3.11). The specific configuration of the cloud computer included a CPU-6-core E5-2680 v4, GPU-RTX 3060 with 12.6 GB VRAM, and 30.1 GB memory. The basic source code and some sample data used in this model training can be found in the author's GitHub repository: https://github.com/ninndesu/ResNet-18-PTF-AFC/.

2.3.2. Gradient-weighted class activation mapping (Grad-CAM)

After the construction of simulation models for thermal anomalies occurrences and their daily/seasonal variations, this study delved further into exploring the nonlinear relations between urban morphology and thermal anomalies using interpretable machine learning. The Grad-CAM (Gradient-weighted Class Activation Mapping) model (Selvaraju et al) was leveraged for this purpose. Urban morphology factors associated with urban thermal anomalies were identified with the assistance of Grad-CAM. Serving as an attention heatmap technique for visualizing neural network models (Fig. 4), Grad-CAM's primary utility lay in the comprehension aid it provided for the model's simulation process. Specifically, it revealed crucial areas of focus within the image, particularly beneficial in image classification tasks. The formula for obtaining neuron importance weights through Global Average Pooling in this algorithm was as follows:

$$\alpha_k^c = \frac{1}{Z}\sum i \sum j \frac{\partial y^c}{\partial A_{ij}^k}$$

where Z represented the number of pixels in the feature map and A_{ij}^k represented the pixel value of the k^{th} feature map in position *(i, j)*. Afterwards, weighting the features of the selected convolutional layer using the neuron importance weights (heatmap) obtained above:

$$L_{Grad-CAM}^c = ReLU\left(\sum k\alpha_k^c A^k\right)$$

In turn, this offered a means to explain model decisions. In this study, our focus primarily rested on quantitatively analyzing the numerical distribution of urban morphology-related indicators in different heat-value regions of the Attention Heatmap, elucidating the spatial correlation between urban morphology and thermal anomaly events (Selvaraju et al).

In the specific course of this study, we: ①Extracted feature maps from various convolutional layers through the forward propagation of deep learning models. ②Identified the target categories for model classification (e.g., urban cold islands, heat islands occurring during specific seasons or timeframes) and computed the gradients for each feature map via backpropagation and gradient computation in relation to these target categories. ③Conducted pooling operations on these gradients, typically employing Global Average Pooling, to obtain weights for each feature map, reflecting the significance of the target categories concerning these feature maps. ④Subsequently multiplied the feature maps by their corresponding gradient weights to obtain weighted feature maps. These weighted feature maps were considered the model's "focus" areas for the target categories and were transformed into heatmaps using normalization and visualization techniques, highlighting the model's areas of interest within the image.

Thus, interpreting convolutional neural network model simulations regarding the occurrence of urban thermal anomaly events in specific remote sensing image slices based on urban morphology constituted the essence of this approach towards interpretable machine learning. It's imperative to note that during the practical experimentation, we conducted resampling of Grad-CAM heat values on the feature map heatmap using a 7*7 grid size. Subsequently, we analyzed the correlation between urban morphology indicators and Grad-CAM heat values for each grid unit within the 7*7 grid. All these processes were executed using

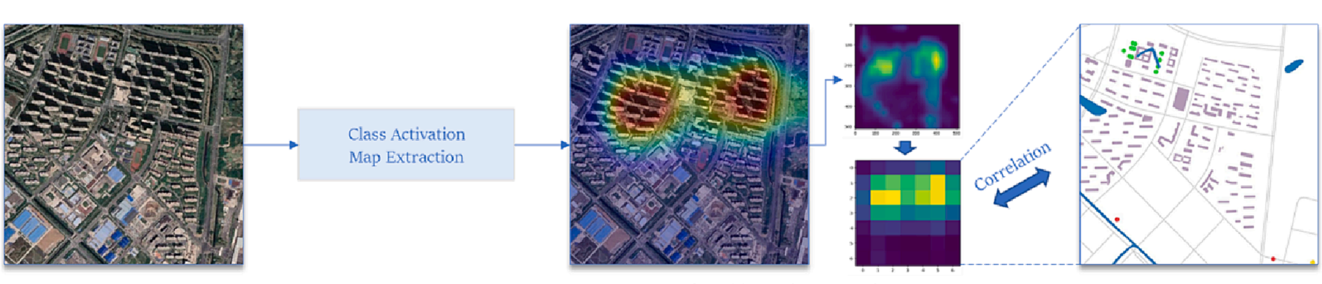

Fig. 4. Procedure of Grad-CAM-based identification of morphology factors related to thermal anomalies.

cloud-based GPUs, with detailed settings and relevant code examples elaborated in section 2.3.1.

2.3.3. XGBoost and SHAP

After completing the identification of urban morphology factors affecting thermal anomalies, this study further modeled the nonlinear relationship between the two with the help of the XGBoost (eXtreme Gradient Boosting), and visualized and interpreted the modeling nonlinear results with SHAP (SHapley Additive exPlanation). XGBoost was a machine learning algorithm that resided in the GBDT (Gradient Boosting Decision Trees) improvement. Different from GBDT, XGBoost added regularization terms to the loss function, and since some loss functions were difficult to compute derivatives, XGBoost utilized a second-order Taylor expansion of the loss function as a fit to the loss function. For a dataset containing n entries of m dimensions, the model could be represented as (Parsa, 2020).

$$\hat{y_i} = \sum_{k=1}^{K} f_k(x_i), f_k \in F(i = 1, 2, \cdots n)$$

In the above equation, $F = \{f(x) = w_{q(x)}\}(q : R^m \rightarrow \{1, 2, \cdots T\}, w \in R^T)$. In the above formula, F represented the set of *CART* decision tree structures; q represented the tree structure of samples mapped to leaf nodes; T represented the number of leaf nodes, and w represented the real fraction of leaf nodes. When constructing the XGBoost model, it was necessary to find the optimal parameters according to the principle of minimizing the objective function in order to build the optimal model. After optimizing the training loss function and regularization penalty term, the final model objective function was obtained as follows:

$$Obj = \sum_{j-1}^{T} \left[G_j w_j + \frac{1}{2}(H_j + \lambda) w_j^2 \right] + \gamma T$$

In the above equation, G_j and H_j represented the sum of the first-order partial derivatives and second-order partial derivatives of the samples contained in leaf node j; λ represented the regularized penalty coefficient; γ represented the decreasing value of the minimum training loss function; w_j^2 represented the square of the weight at leaf node j.

After completing the training and optimization of the XGBoost model, this study further explained the nonlinear relationship between urban morphology and thermal anomalies visually by using SHAP, a game-theoretic method. This method constituted the core idea for calculating the marginal contribution of features to the model output and subsequently explaining the 'black-box model' at both global and local levels. The contribution of each feature to the model output was assigned based on its marginal contribution, and the SHAP value was determined by the following equation:

$$\varnothing_i = \sum_{S \subseteq N\{i\}} \frac{|S|!(|N| - |S| - 1)!}{|N|!} [v(S \cup \{i\}) - v(S)]$$

In the above equation, $\varnothing_i$ represented the SHAP value of feature i; N represented the sample feature vectors to be interpreted; S represented the vector of feature combinations that do not contain feature i in the sample feature vector N; $v(S \cup \{i\})$ and $v(S)$ represented the model output values with and without the effect of feature i, respectively. All above XGBoost model training and testing and SHAP processes were executed using cloud-based GPUs (elaborated in section 2.3.1). To be specific, tthis study formulated the XGBoost regression model utilizing Grad-CAM heat values from the thermal anomalies simulation model at resampled pixel locations as the dependent variable, while urban morphology factors served as the independent variables.

3. Results

3.1. Accuracy of thermal anomalies simulation

3.1.1. General accuracy performance

Three fine-grained image classifiers were built with the ResNet-18 alongside transfer learning algorithms for urban thermal anomalies simulation. The primary objective was to enhance the accuracy of simulating urban thermal anomalies based on remote sensing images. Table 1 outlined the specific performance factors of the constructed models.

Initially, in the first model, ResNet-18-PTT-FFC, only the parameters of the last fully connected layer were fine-tuned while other layers were kept frozen. Subsequently, the second model, ResNet-18-PTT-AFC, emerged as we fine-tuned all layers of the pre-trained ResNet-18 model. Lastly, the third model, ResNet-18-PTF-AFC, was obtained by training all layers from scratch without utilizing pre-trained weight parameters. A thorough comparison of these transfer learning models in simulating urban thermal anomalies revealed the relatively superior performance of ResNet-18-PTF-AFC. Within a test set of 12,089 remote sensing image slices covering Nanjing's downtown area, this model accurately identified urban thermal anomalies in 9,614 corresponding grid cells, achieving an overall accuracy of 79.52 %. Notably, ResNet-18-PTF-AFC exhibited a 1.61 % and 1.39 % improvement over ResNet-18-PTT-AFC in simulating urban heat and cold islands, respectively. In comparison to ResNet-18-PTT-FF, it demonstrated performance enhancements of 3.26 % and 7.15 % in the same aspects. Afterwards, the ResNet-18-PTF-AFC model was applied to simulate urban thermal anomalies' occurrences within Shanghai's central area for 2018, as depicted in Fig. 5. The test set comprised 60,450 distinct remote sensing image slices, varying in dimensions, portraying instances of urban thermal anomalies (heat or cold islands). Fig. 5 utilized varying shades of red and blue to represent the frequency of recording or simulating these anomalies, with deeper shades denoting a higher occurrence within the specified region.

The model's performance closely aligned between the test set (Shanghai area) and the validation set (Nanjing area), which achieved an approximate 80.42 % accuracy in simulating urban thermal anomalies in Shanghai (Table 2). Specifically, the ResNet-18-PTF-AFC model, obtained through transfer learning, exhibited exceptional performance in simulating regions prone to thermal anomaly events (where the annual average temperature consistently approached the regional mean), surpassing 88.42 % accuracy (as shown in the third column of Fig. 5). However, in simulating urban cold spots, its performance was relatively weaker, with an accuracy of 65.99 %, slightly lower than the 76.47 % observed in the validation set (as seen in the second column of Fig. 5). Notably, deviations existed between the simulated pattern of urban cold spots by ResNet-18-PTF-AFC and the ground truth. Conversely, for simulating urban heat spots, the model demonstrated balanced performance, achieving 75.51 % accuracy. A comparison between the ground truth heat spot pattern (first column of Fig. 5) and the model's simulation results revealed a close overall resemblance, with minor discrepancies in details.

3.1.2. Accuracy performance of the models with RS images in different resolutions

After testing various transfer learning approaches and establishing a highly accurate model for simulating urban thermal anomalies, this study compared the effectiveness of different-sized remote sensing image slices in simulating urban heat islands and cold islands within urban central spaces. The results were presented in Table 2.

The findings revealed that oversized dimensions might have encompassed excessive geographical features, hindering accurate simulations of urban thermal anomalies. For instance, the simulation accuracies of image slices at 750 m and 1500 m dimensions, evaluated with ResNet-18-PTF-AFC on the test set, were only 73.32 % and 75.43

Table 1
General performance of models trained to simulate thermal anomalies.

Model Type	AVG		UCI		UHI		OVERALL	
	Grids	Accuracy	Grids	Accuracy	Grids	Accuracy	Grids	Accuracy
ResNet-18-PTT-FFC	6972	81.32 %	834	69.32 %	1723	74.53 %	9529	78.82 %
ResNet-18-PTT-AFC	6924	80.76 %	903	75.08 %	1761	76.18 %	9588	79.31 %
ResNet-18-PTF-AFC	6895	80.41 %	920	76.47 %	1799	77.79 %	9614	79.52 %

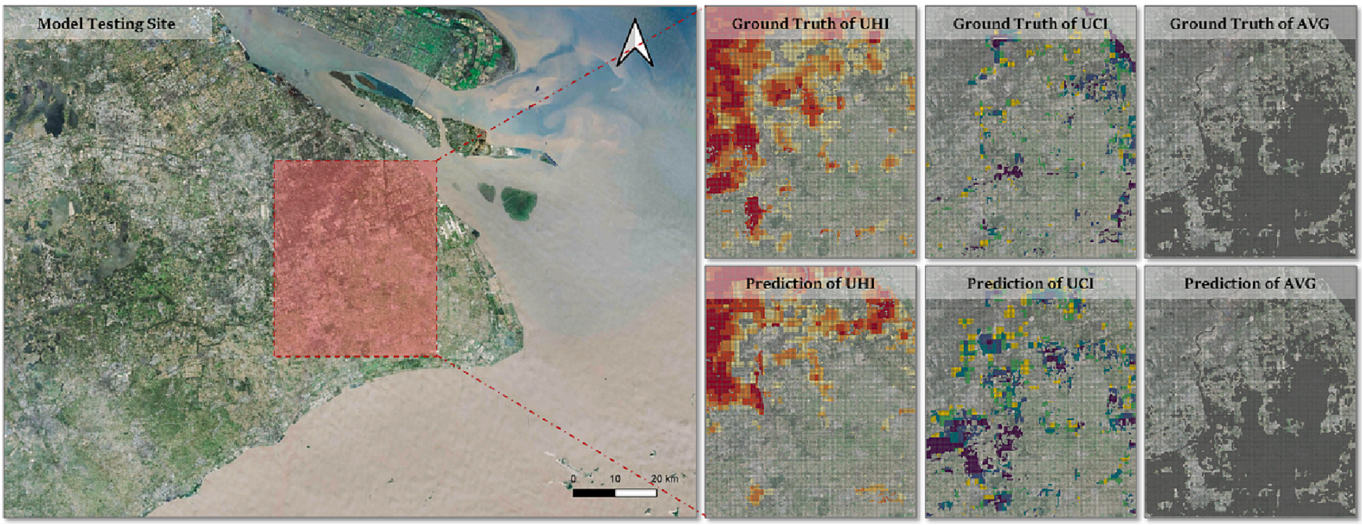

Fig. 5. Performance of ResNet-18-PTF-AFC model in thermal anomalies simulation.

Table 2
Performance of models with RS images in different resolutions.

Resolutions	AVG		UCI		UHI		OVERALL	
	Correct	All	Correct	All	Correct	All	Correct	All
250 *m*	11,868 (88.43 %)	13,421	2042 (65.25 %)	3130	9450 (75.81 %)	12,465	23,360 (80.51 %)	29,016
300 *m*	8165 (88.03 %)	9275	1505 (67.42 %)	2233	6635 (76.78 %)	8642	16,305 (80.92 %)	20,150
500 *m*	3042 (91.56 %)	3322	550 (68.90 %)	798	2390 (76.25 %)	3134	5982 (82.46 %)	7254
750 *m*	1274 (85.76 %)	1485	214 (65.25 %)	351	876 (75.81 %)	1388	2364 (73.32 %)	3224
1500 *m*	308 (83.15 %)	370	106 (58.33 %)	181	194 (75.97 %)	255	608 (75.43 %)	806

%, respectively. However, the three remaining sizes demonstrated simulation accuracies surpassing 80 %. Notably, the 500 m-sized remote sensing image slices exhibited the highest performance on the test set, achieving an overall simulation accuracy of 82.46 %. These 500 m-sized slices outperformed other sizes in simulating whether urban temperatures matched the annual average and in identifying urban cold islands. Their simulation accuracy for urban heat islands was slightly lower, by only 0.53 %, compared to the 300 m-sized remote sensing image slices. Consequently, the subsequent phases of this study continued utilizing the 500 m-sized remote sensing image slices to enhance research outcome accuracy.

3.1.3. Accuracy performance of the models in different simulation scenarios

The ResNet-18-PTF-AFC model not only simulated the occurrence of thermal anomalies such as urban heat islands and cold islands in remote sensing images but also forecasted their timing (day or night) and seasonality (summer or winter). Consequently, this research further compared the performance of the ResNet-18-PTF-AFC model in simulating thermal anomalies during different time periods and seasons. Comparative results were summarized below (Table 3).

The research findings indicated that discrepancies were notably observed among seasons, with winter showing an average increase in accuracy of approximately 2.02 % in simulating urban thermal anomaly events over summer. However, no significant differences were evident between day and night simulations. Further comparisons revealed that the model demonstrated superior performance in forecasting urban heat islands during winter (an increase of around 3.05 %) but excelled in simulating urban cold island occurrences during summer (with an approximate 4.08 % increase). Regardless of whether the model simulated cold or heat island events, these performance variations persisted only between different seasons.

3.2. Identification of morphology factors related to thermal anomalies

After finalizing the construction and accuracy validating of the thermal anomalies simulation model, Grad-CAM was employed in this study to elucidate the key mechanisms within the ResNet-18-PTF-AFC model (at 500-meter resolution) during simulating thermal anomalies.

Table 3
Performance of models in different simulation scenarios.

Scenarios	AVG		UCI		UHI		OVERALL	
	Correct	All	Correct	All	Correct	All	Correct	All
Summer Daytime	4383 (85.35 %)	5135	130 (69.82 %)	186	1421 (73.53 %)	1933	5934 (81.80 %)	7254
Summer Nighttime	4398 (85.65 %)	5135	193 (69.32 %)	279	1348 (73.28 %)	1840	5939 (81.87 %)	7254
Winter Daytime	4557 (88.74 %)	5135	651 (65.33 %)	997	858 (76.50 %)	1122	6066 (83.62 %)	7254
Winter Nighttime	4584 (89.27 %)	5135	632 (65.66 %)	962	884 (76.41 %)	1157	6100 (84.09 %)	7254

The primary focus lay in pinpointing pivotal pixels within remote sensing imagery slices that exerted influence on the model's simulation judgments was further summarized to clarify the factors related to thermal anomalies within different time spans and seasonal variations. Specifically, Grad-CAM was utilized to visualize the process by which predictions were made by the ResNet-18-PTF-AFC model. The key pixels that influenced the model's formation of judgments were displayed in the form of heatmap, as shown in the activation map in rows 2–3 of Figs. 6 and 7.

3.2.1. *Morphology factors related to thermal anomalies within different scenarios*

Initially, the differences in the remote sensing imagery pixel regions of model response were compared under various simulations scenarios (different urban thermal anomalies event types). Fig. 6 illustrated hotspot regions of interest identified by Grad-CAM for the ResNet-18-PTF-AFC model in scenarios depicting no thermal anomaly, urban cold island presence, and urban heat island presence. The resulting findings could be summarized as follows:

(1) Regions characterized by extensive green coverage (Region 6–4) and low-density, dispersed building areas (Regions 6–1, 6–2, 6–3) were less susceptible to the urban heat island and cold island phenomena. Abundant green spaces, teeming with vegetation and soil, efficiently absorbed solar energy and promoted significant ventilation, enabling proficient heat exchange with the surrounding environment. Unlike densely populated urban areas, zones featuring low-density, scattered buildings generally provided increased open spaces and greenery, encouraging improved air circulation and reducing the occurrence of thermal anomalies.

(2) Urban cold island occurrences were more prevalent in specific regions characterized by shaded, densely populated, low-lying streets (Region 6–5), areas adjacent to wetlands and water bodies (Regions 6–6, 6–7), and shadowed zones amidst tall buildings (Region 6–8). These locations, such as narrow streets shielded by towering structures, experienced limited direct sunlight exposure, leading to decreased local temperatures. Wetlands and water bodies played a significant role in moderating ambient temperatures by absorbing and releasing heat, thereby inducing cooler microclimates in their vicinity, resulting in the formation of cold islands. Furthermore, diminished sunlight penetration caused by tall structures or other obstacles contributed to the lowered temperatures observed in these regions.

(3) Urban heat island occurrences were more commonly observed in specific regions, such as industrial zones (Region 6–9), commercial districts (Region 6–10), high-density constructions (Region 6–11), and densely populated areas (Region 6–12). These areas frequently housed multiple factories, machinery, and vehicular activities, resulting in the emission of substantial waste heat and exhaust gases, thereby raising temperatures within their confines. The concentrated structures of high-density constructions and densely populated areas impeded air circulation, impeding the efficient dissipation of heat. Additionally, these areas experienced significant vehicular emissions, further contributing to elevated temperatures. Compounded by the absence of water bodies and wetlands, these regions struggled to regulate ambient temperatures adequately, ultimately fostering the formation of urban heat islands.

3.2.2. *Morphology factors related to thermal anomalies within different time pierids*

Subsequently, the differences in the remote sensing image pixel regions of model response were compared within different time periods and seasons. Fig. 7 illustrated the identified hotspot regions of interest highlighted by Grad-CAM in summer/winter during daytime and nighttime. The resulting findings could be summarized as follows:

(1) The urban heat island effect was notably pronounced in specific zones throughout different seasons. During summer, it was more prevalent in the central business districts (Region 7–3), high-density residential areas (Regions 7–4, 7–7), and industrial regions (Region 7–8). In contrast, winter exhibited a prominence of the heat island effect in urban commercial areas, especially during cold and clear weather conditions (Region 7–11). Seasonal

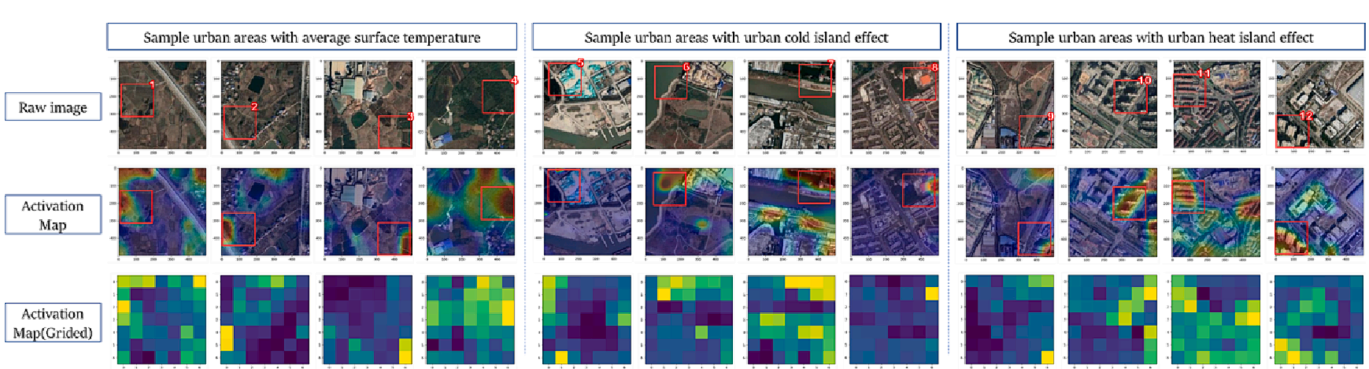

Fig. 6. Sample focal pixel regions in Grad-CAM (within different scenarios).

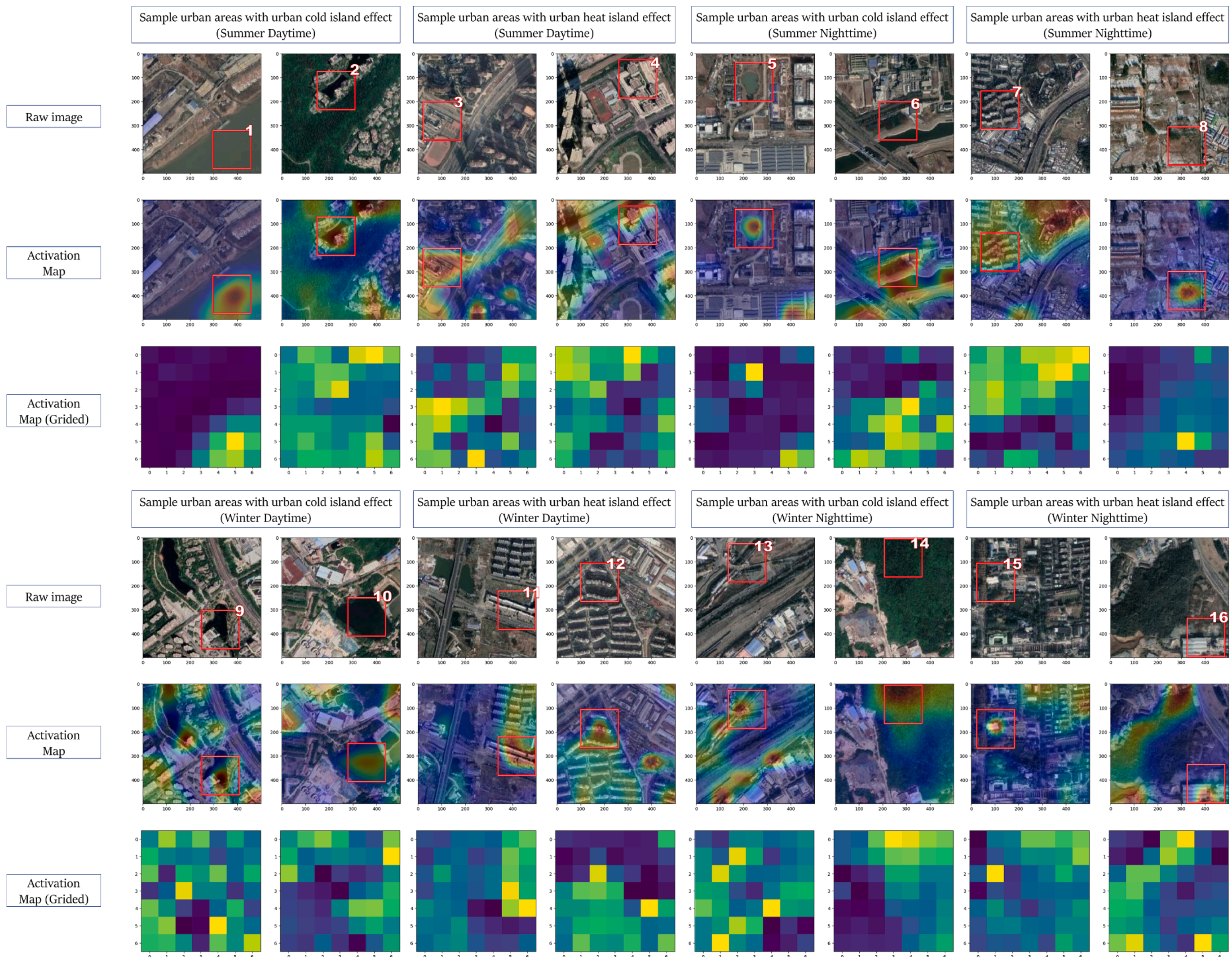

Fig. 7. Sample focal pixel regions in Grad-CAM (within different time).

variations in this effect were influenced by factors such as city building density, human activities, climate conditions, and solar radiation.

(2) The emergence of a cold island phenomenon was associated with proximity to sizable water bodies within urban landscapes (Regions 7–1, 7–2, 7–5) and waterfront areas (Region 7–6) during summer. Conversely, during winter, this effect was typically observed in high-rise urban areas (Region 7–9), open spaces on the urban periphery (Region 7–13), or areas characterized by extensive vegetation cover (Region 7–14), particularly on calm and clear nights. Seasonal variations in the cold island effect were closely tied to factors such as climate, topography, and vegetation cover.

(3) The daytime urban heat island effect was typically observed in central business districts (Regions 7–3, 7–11) and high-density office building areas (Region 7–4). In contrast, the nighttime urban heat island effect tended to dominate in the city's industrial zones (Regions 7–8, 7–16). This phenomenon was mainly attributed to the varying absorption and release of energy within the city throughout the day and night.

(4) The daytime urban cold island effect tended to be more pronounced in proximity to extensive lakes, rivers (Regions 7–1, 7–10), and developed waterfront areas (Regions 7–2, 7–9). Conversely, the nighttime urban cold island effect was more evident in artificial structural environments, such as outskirts roadways (Region 7–13) or areas characterized by substantial vegetation cover (Region 7–14). This discrepancy arose from variations in the processes of heat absorption and release across different locations.

In general, the ResNet-18-PTF-AFC model, alongside Grad-CAM, delineated associations between thermal anomalies and diverse urban morphology factors across various event types and temporal scenarios. Strong correlations with thermal anomalies emerged in specific urban areas, namely: ①Urban blue (water bodies) and green spaces (urban forests, grasslands, and parks); ②Urban transportation infrastructure (railways, stations, and roads); ③High-density urban commercial and residential zones; ④Urban industrial areas, social facilities, production centers, and amenities. Furthermore, the identification of dominant factors was contingent upon the timing of thermal anomaly occurrences.

3.2.3. Validation of the results of key morphology factor identification

This study verified the robustness of identifying key urban morphology factors affecting thermal anomalies via Grad-CAM by resampling the weighted feature maps onto a 7*7 grid (details in Section 2.3.2). And the Pearson correlation analysis was employed to evaluate the relationship between Grad-CAM heat values of the weighted feature maps at each grid and corresponding urban built environment characteristics (see Section 2.2.3). Fig. 8's Pearson correlation outcomes consistently aligned with Grad-CAM model response regions on urban remote sensing imagery slices in Sections 3.2.1 and 3.2.2. All urban built environment elements showed varying degrees of correlation with thermal anomalies under at least one scenario. Among morphology factors, GS and WS exhibited the strongest associations with thermal anomalies, displaying the highest Pearson correlation coefficients (0.64 and 0.615, respectively) with eigenvalues of the summer urban heat island. LIF followed, showing the highest correlation coefficient (0.732) with eigenvalues of the summer night urban heat island under the full scenario, slightly lower on average than GS and WS. PRO, reflecting industrial and socially productive land characteristics, exhibited correlation coefficients between 0.392 and 0.449, especially evident in summer. SOC, BD, and RD showed slightly lower Pearson correlations with thermal anomalies compared to the aforementioned factors, maintaining an average correlation level of over 0.2, particularly noticeable in summer.

When comparing scenarios, Pearson correlation analysis indicated a notably stronger association between urban morphology and thermal anomalies in summer than in winter, with an average coefficient increase of about 0.183. Moreover, the correlation between morphology factors and heat island regions' Grad-CAM heatmap eigenvalues demonstrated a more pronounced response mechanism, with an average coefficient increase of approximately 0.139.

3.3. Nonlinear relations between morphology and thermal anomalies with threshold effect

After identifying and validating urban morphology factors associated with thermal anomalies using Grad-CAM, this study formulated the XGBoost regression model. It utilized Grad-CAM heat values from the thermal anomalies simulation model at resampled pixel locations as the dependent variable, while urban morphology factors served as the independent variables. The XGBoost models simulated urban thermal anomalies across 8 scenarios, with an average mean squared error (MSE) ranging from 0.001 to 0.003. Additionally, SHAP was employed to visualize and analyze the nonlinear regression process, primarily focusing on nonlinear patterns, activation levels, and threshold effects.

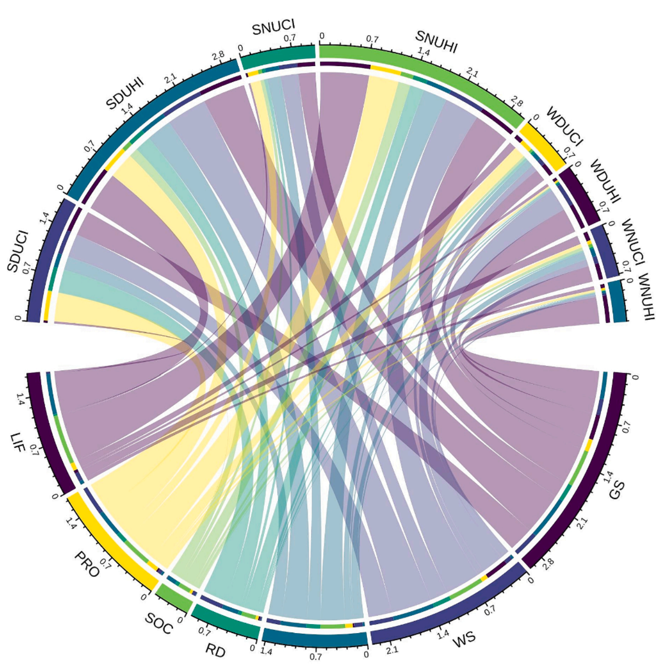

Fig. 8. Pearson correlations between urban morphology factors and thermal anomalies.

3.3.1. Importance order of urban morphology factors affecting thermal anomalies

The XGBoost model was further adapted to incorporate the SHAP interpreter, and the SHAP values related to urban morphology feature variables were sorted and visualized. This ranking illustrated the contribution of urban morphology factors to thermal anomaly simulation results.

Fig. 9 demonstrated the comprehensive relationship between variables characterizing each urban morphology factor. Each data point on the graph represented a sample object, with distinct colors denoting original high or low values of the respective feature variable. The horizontal axis represented the SHAP value, indicating the magnitude of influence exerted by the feature variable on the XGBoost model outcomes. A positive SHAP value indicated a positive contribution of the urban morphological feature variable to thermal anomalies, while a negative value signified an inhibitory effect. As shown in Fig. 9, the combined impact of green spaces area (GS), water space area (WS), spatial arrangements of essential living and residential facilities (LIF) such as office buildings and commercial zones, building floor area ratio (BD), and the distribution of industrial production facilities (PRO) emerged as crucial factors that contributed to thermal anomalies within the city. Their average SHAP value contributions were notably higher than those of other urban morphology indicators.

Significant variability was observed in the SHAP values corresponding to each urban morphology characterization variable across different times. During winter, GS showed significantly stronger associations with urban thermal anomalies compared to summer, with mean SHAP influence orders 4.5 places higher. Conversely, BD exhibited heightened associations with thermal anomalies during summer, with mean influence orders 2 places higher. Differences in SHAP values between daytime and nighttime indicated significant variations in the mechanisms linking urban morphology to urban thermal anomalies at different time periods. RD displayed notably stronger correlations with urban thermal anomalies during the daytime, with mean influence orders 1.5 places higher than during the nighttime, while BD showed heightened associations with thermal anomalies during the nighttime, with mean influence orders 1.5 places higher.

When evaluating various urban thermal anomaly events in relation to urban morphology, the ranking of SHAP values revealed varied results, particularly in BD, WS, and SOC indicators. Specifically, the BD factor significantly affected the mitigation of the urban cold island effect but showed relatively lower significance in contributing to the urban heat island, with an average SHAP value importance order difference of 3.5 places of magnitude. In contrast, WS and SOC had a more substantial impact on the urban heat island effect compared to the cold island.

Furthermore, the analysis of SHAP value contributions highlighted instances where urban morphology factors might have outliers in promoting or suppressing effects on the same type of thermal anomalies in specific different scenarios. For example, BD had a localized promoting effect on the urban cold island phenomenon (dark-colored scatters of BD in Fig. 9-e were distributed within the coordinate interval with positive SHAP values). Similarly, LIF also promoted the urban cold island phenomenon in extreme summer scenarios (light-colored scatters of LIF in Fig. 9-a were distributed within the coordinate interval with positive SHAP values). These findings were contrary to other scenarios significantly.

3.3.2. Nonlinear mechanism of urban morphology's impact on thermal anomalies

Finally, the study plotted partial dependency diagrams (PDPs) of the XGBoost model using SHAP to visualize the nonlinear relationships between the most vital (top 2 in SHAP values) urban morphology factors and thermal anomalies in various seasons, time periods, and scenarios of thermal anomaly types. The results were presented in Fig. 10. Specifically, our study directed attention towards the patterns, activations, and thresholds represented by the scattered points and folded lines

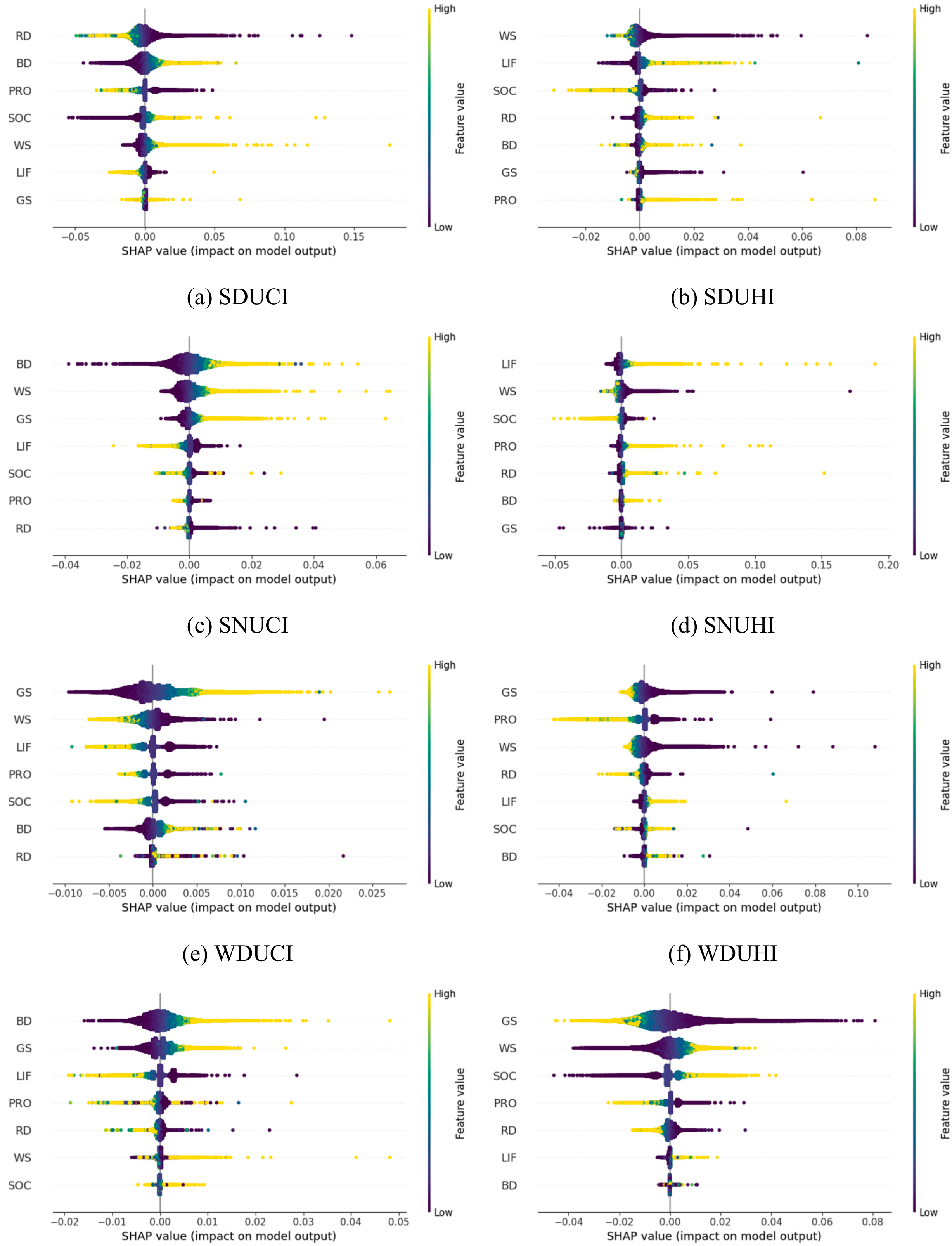

(a) SDUCI (b) SDUHI

(c) SNUCI (d) SNUHI

(e) WDUCI (f) WDUHI

(g) WNUCI (h) WNUHI

Fig. 9. Importance of SHAP values regarding urban morphology factors.

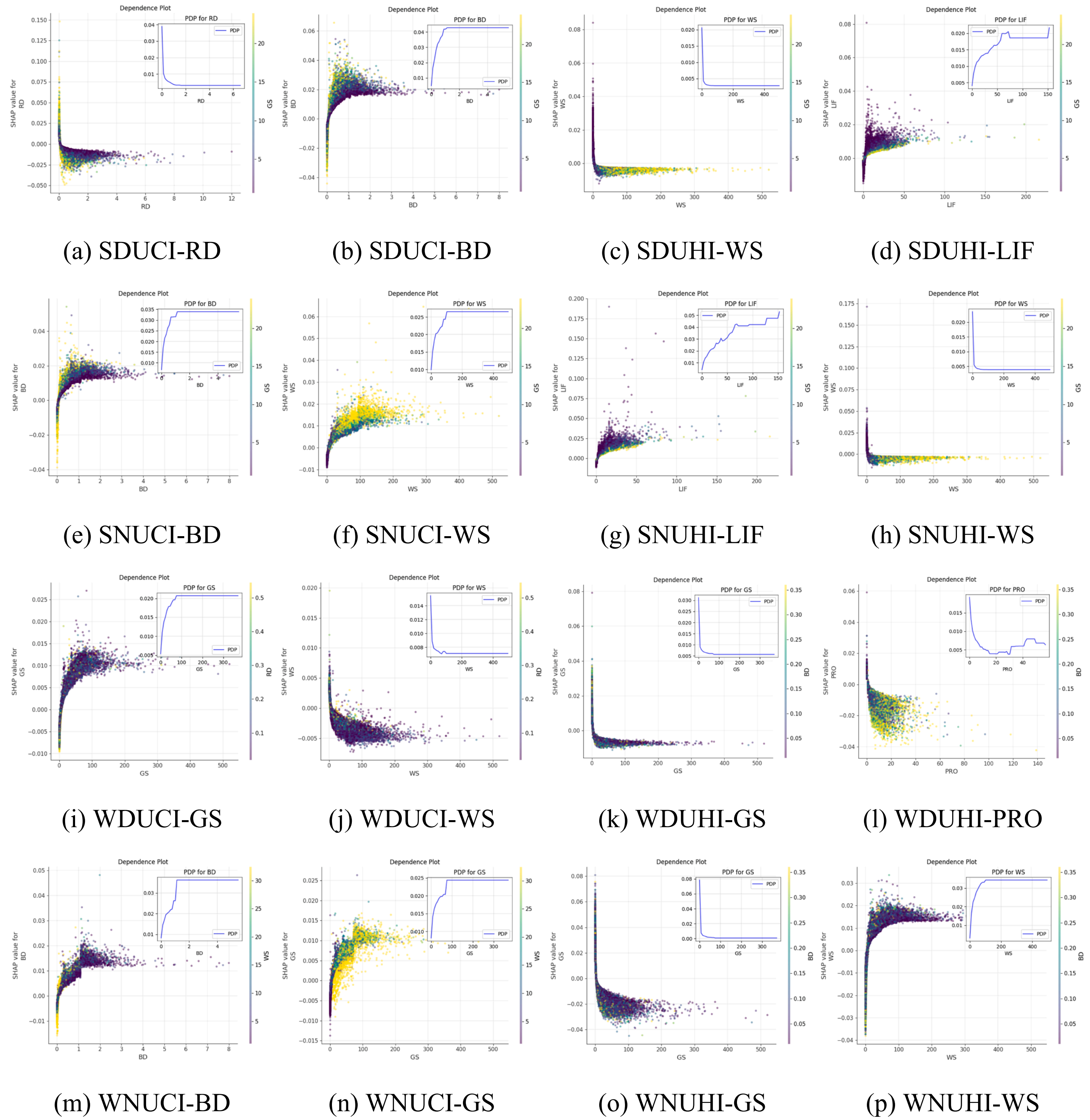

Fig. 10. Partial dependence analysis of urban morphology factors.

within these plots. These elements laid the foundation for interpreting the nonlinear relationship observed between urban morphology indicators and thermal anomalies.

a. Green space area.

The results of fitting the nonlinear relationship for indicator GS (Green Space Area) demonstrated that an urban space of approximately 520 m^2 exhibited a greater occurrence of an urban cold island with an increase in the green space area, varying from 0 to 90 m^2. A significant threshold was observed at the 90 m^2 level, beyond which the occurrence of urban cold islands remained unaffected by changes in the green space area. It was noteworthy that for the urban cold island phenomenon at night, an activation level was evident at 75 m^2. Upon reaching 75 m^2, the increase in its area substantially augmented the occurrence of the cold island until it surpassed 90 m^2. The relationship between urban heat island and GS demonstrated a higher level of complexity, manifesting two significant thresholds in the PDP plot. The initial threshold appeared at 9 m^2, where an augmentation in green space area significantly diminished the occurrence of heat islands as the regional green space area varied from 0 to 9 m^2. With the green space area increasing from 9 to 88 m^2, the probability of a heat island's occurrence still diminished, albeit at a notably slower pace. Ultimately, upon reaching the second threshold of 88 m^2, alterations in green space area ceased to affect the emergence of heat islands. The observed nonlinear relationships between GS and thermal anomalies, as delineated above, were notably more pronounced during winter.

b. Number of living and residential facilities

The nonlinear relationship between the number of living and residential facilities (LIF), identified as a core urban morphology factor impacting thermal anomalies, demonstrated a significant association between changes in its eigenvalues and the urban heat island (UHI) phenomenon. Two distinct thresholds were evident in the overall fitting results of the nonlinear relationship between LIF and the probability of UHI occurrence. The first threshold manifested within the range of 68–70, where the probability of UHI occurrence increased with rising LIF values from 0 to approximately 68. Subsequently, the probability stabilized upon reaching the first threshold. The second threshold, observed within the range of 130–147, showed insignificant fluctuations in UHI probability as the LIF indicator varied between 68 and approached 147. Beyond the second threshold at 147, a notable increase in UHI occurrence was witnessed with rising LIF values, surpassing the rate observed within the 0 to 68 range. Moreover, the fitting results of the nonlinear relationship between LIF factors and UHI exhibited localized differences between daytime and nighttime scenarios during summer. In the daytime scenario, UHI probability exhibited minimal variation as the LIF factor ascended towards the first threshold at 68, stabilized briefly until 72, and experienced a marginal decrease of approximately 0.5 % between 72 and 73 before stabilizing again until the second threshold at 137. Conversely, in the nighttime scenario, the LIF indicator underwent slight fluctuations until reaching the second threshold at 137, remaining relatively stable around 127 thereafter, corresponding to a rise in UHI probability.

c. Building floor area ratio.

The strong consistency in fitting results across scenarios revealed a nonlinear correlation between building floor area ratio (BD) and urban thermal anomalies. Regarding the urban heat island phenomenon, a rapid increase in occurrence was observed with rising BD indicator values between 0 and 1.1. However, beyond a BD of 1.1, changes in the factor value no longer impacted the occurrence of the urban heat island. Conversely, concerning the urban cold island, a swift decrease in occurrence occurred as the BD factor rose from 0 to 1.3. Yet, beyond a BD of 1.3, alterations in its factor value ceased to affect the occurrence of urban heat islands. Moreover, this study identified an unexpected observation regarding the BD factor's influence on the probability of urban cold island occurrence during summer and winter scenarios. In the summer, contrary to expectations, the probability of urban cold island occurrence escalated with increasing BD factor values until reaching the first threshold of 1.3. This intriguing finding was extensively discussed in the study's subsequent Discussions section 4.1 and 4.2.

d. Road density.

A significant nonlinear relationship was identified between the emergence of urban heat islands during daytime in summer and RD (Road Density), revealing a notable threshold. As road density increased from 0 to 1.2 km per square kilometer, a decrease in the occurrence of urban heat islands was observed. This decline demonstrated an inverse correlation between road density and the occurrence of urban heat islands. Notably, a significant threshold was evident at the 1.2-kilometer mark. Subsequent to surpassing this threshold, changes in the area of green space no longer affected the occurrence of urban heat islands.

e. Number of industrial production facilities

A significant nonlinear relationship existed between the number of industrial production facilities (PRO) and the urban heat island during winter daytime. Two significant thresholds, along with several activation levels, were observed. The initial threshold, at 16, exhibited a marked decrease in the occurrence of the heat island as the PRO ranged from 0 to 16. As the number of industrial production facilities increased from 16 to 44, the probability of a heat island occurrence rose with an increasing PRO, albeit at a considerably slower rate. Upon surpassing the second threshold of 44, a rise in the PRO factor once again showcased a mitigating effect on the probability of an urban heat island emergence. Importantly, at least three activation levels were identified at 33, 41, and 52. When the number of industrial production facilities reached 33 and 41, the impact of PRO increase on the heat island occurrence accelerated significantly until the PRO value exceeded the threshold level of 44. Conversely, upon reaching the activation level of 52, the impact of PRO increase on the heat island occurrence diminished more rapidly.

f. Water space area.

The intricate nonlinear relationship between watershed area (WS) and urban thermal anomalies yielded contrasting outcomes across different time periods. In the case of thermal anomalies like urban heat islands, a consistent trend emerged across a majority of scenarios: a gradual decrease in event occurrence was observed with increasing watershed area, revealing two notable threshold effects. The initial threshold, at 6 m^2, marked a pronounced decrease in the occurrence of heat islands as WS ranged from 0 to 6 m^2. Subsequently, as the water space area extended from 6 to 69 m^2, the likelihood of a heat island occurrence diminished with increasing WS, albeit at a slower pace. Once surpassing the second threshold of 69 m^2, any rise in the PRO factor no longer significantly influenced the probability of urban heat island emergence. Regarding urban cold islands, a consistent trend also emerged across most scenarios: a gradual increase in event occurrence was observed with increasing watershed area, marked by one significant threshold and an activation level. The nonlinear relationship analysis for the WS factor revealed a higher occurrence of urban cold islands with an expansion in water space area, ranging from 0 to 106 m2. A notable threshold was identified at the 106 m^2 level, beyond which the occurrence of urban cold islands remained unaffected by changes in green space area. Importantly, an activation level was discernible at 28 m^2. Upon reaching this threshold, the incremental increase in water area minimally impacted the occurrence of the cold island until it surpassed 106 m^2.

Moreover, an inverse nonlinear relationship existed between WS and urban thermal anomalies, contrasting with patterns observed in other seasons in winter. For instance, during winter nights, the urban heat island occurrence escalated, contrary to decreasing trends, in proportion to the regional watershed area until a critical threshold (at 135 m^2) was reached, beyond which it ceased to impact thermal anomalies. Similarly, daytime occurrences of urban cold islands decreased, in contrast to expected increases, with the expansion of the regional watershed area until a threshold (at 78 m^2) was attained, marking a point where its influence on thermal anomalies diminished. Notably, urban cold island occurrences displayed minor fluctuations within the 78–82 m^2 range of watershed area.

It was further emphasized that despite having been recognized as an influential factor on urban thermal anomalies in previous Grad-CAM-based identifications of urban morphology elements and Pearson correlation analysis, SOC (number of social welfare facilities) did not exhibit a significant nonlinear relationship with specific types of thermal anomalies during the targeted seasons and time frames.

4. Discussions

In this study, crucial insights into seasonal and daily variations in the correlations between urban morphology and thermal anomalies were uncovered. Two significant breakthroughs were made. Firstly, a proficient ResNet-18-PTF-AFC model was developed using CNNs and transfer learning techniques to simulate urban thermal anomalies from remote sensing imagery data. Secondly, it unveiled the intricate nonlinear connection between thermal anomalies and urban morphology. Specifically, spatial correlations of urban elements with thermal anomalies were investigated using the interpretability of Grad-CAM and SHAP algorithms. This method facilitated the visual delineation of pixel regions associated with urban thermal anomaly simulation, aiding the identification of key urban features emphasized during classification and revealing the threshold effect within the nonlinear trend. Within these pivotal findings, two noteworthy points warrant attention.

4.1. Linkage between dense high-rise residential buildings and summer urban cold island

In Section 3.3, insights gleaned from Grad-CAM interpretability analysis revealed that, in the context of simulating the likelihood of urban cold islands occurring in corresponding urban areas during winter using remote sensing images, the ResNet-18-PTF-AFC model primarily focused its attention on image pixel regions within high-rise residential areas. This pixel-based observation indirectly implied a potential correlation between the presence of densely packed high-rise residential buildings and the occurrence of urban cold islands. This finding stood in contrast to conventional research, which commonly posited that high-density cities contributed to the urban heat island effect through increased building structures absorbing solar radiation and emitting heat (Chun and Guldmann, 2014; Li et al., 2020; Terjung and Louie, 1973).

To verify this unexpected correlation, further investigation was conducted in the designated area (Region 7–9) and the distinctive features were unveiled in these densely constructed high-rise residential zones: ①A low overall building density in the surrounding regions; ②significant building volumes and heights; ③remarkably high levels of greenery within residential areas. Consequently, based on these findings, three potential mechanisms linking dense high-rise residential buildings to urban cold islands were inferred: ①High-rise residences predominantly positioned at critical junctures of urban ventilation corridors in the case study area likely experienced stronger wind effects due to surrounding open spaces, resulting in lower temperatures (Yang et al., 2011); ②These buildings surpassed the regional average in both area and height, facilitating increased heat dissipation owing to their larger surface area. Moreover, investigations revealed the predominant use of white or light-colored materials like glass, concrete, and tiles, which were conducive to heat dissipation (Santamouris et al., 2011); ③The target area pertained to a newly developed section of the city primarily inhabited by affluent individuals. Consequently, residential neighborhoods within this area exhibited high levels of green landscapes and a significant presence of vegetation and water bodies, crucial for area cooling and the formation of urban cold islands (Chen et al., 2014).

4.2. Linkage between urban living facilities cause urban cold island in summer

During daytime and nighttime in summer, the quantity of urban living facilities (such as shopping centers, entertainment venues, sports arenas, etc.) displayed a diafactorally opposite nonlinear pattern in weighted Grad-CAM feature map heat values associated with urban cold islands. This observation stood in stark contrast to prior research, which indicated that an increased presence of shopping centers, entertainment venues, and sports arenas within a region amplified the probability of urban heat island effects (Nuruzzaman, 2015; Ojima, 1990). The surrounding temperatures were typically elevated by the use of air conditioning, lighting, and other heat-releasing devices in these facilities. Furthermore, increased population density and heat accumulation were facilitated by their ability to attract larger crowds to the city center (Ramírez-Aguilar and Lucas Souza, 2019; Lemonsu et al., 2015).

To validate this, on-site research was conducted during daytime hours (06:00 to 18:00) at the primary shopping centers and entertainment venues in the study area to measure local temperatures. Instances were observed where local temperatures were found to be lower than the regional average. The analysis, combined with objective observations, suggested that certain shopping centers, entertainment venues, or sports arenas in the study area incorporated highly efficient heat insulation designs. For example, technologies such as double-layer, highly reflective materials, and heat bridge isolation were employed in the external walls, roofs, and floor structures of establishments like the Deji Shopping Mall in Nanjing, resulting in the maintenance of lower internal temperatures compared to the surrounding areas. Furthermore, many facilities in the region operated with superior cooling systems during high summer temperatures, maintaining average interior temperatures considerably lower than the surrounding areas by approximately 14–16 °C during the day, primarily due to air conditioning. During interviews with the responsible personnel, acknowledgment was given to the intentional cooling of malls during summers to attract customers and provide a comfortable environment. However, it was noted that excessive use of air conditioning contributed to energy wastage and environmental burden (Tremeac, 2012).

4.3. Applicability and limitations

The main findings concerning urban morphology and the thermal environment stem primarily from empirical research conducted in cities characterized by a northern subtropical monsoon climate (specifically Nanjing and Shanghai). Notably, the influence of urban morphology on the urban thermal environment exhibited varied mechanisms across different latitudes and climatic regions (Kotharkar and Bagade, 2018). From a latitudinal standpoint, urban thermal anomalies in low latitude regions were predominantly influenced by tropical climates (Yang et al., 2020). These regions typically experienced higher temperatures, leading to increased absorption of solar radiation energy by building and road surfaces during urbanization processes. In mid-latitude regions, urban thermal anomalies may have been more significantly affected by seasonal climate variations (Liu et al., 2020). Conversely, at higher latitudes, urban thermal anomalies may have been more heavily influenced by the materials comprising buildings and roads within the city. In cold climates, these surfaces often accumulated substantial heat, resulting in warmer city interiors relative to the surrounding areas, particularly during winter months. Consideration of different climatic zones revealed that the impact of urban thermal anomalies was subject to additional factors such as climate type, precipitation, and wind speed. In arid climates, urban areas lacking water bodies or vegetation may have exhibited more pronounced urban heat island effects due to reduced evaporative cooling (Lu and Lange, 2024). Conversely, in humid climates, high levels of humidity could have impeded heat dissipation, prolonging the duration of urban thermal anomalies. In oceanic climate zones, the moderating influence of the ocean could have mitigated urban thermal anomalies, particularly during summer months, by slowing the formation of urban heat islands (Yin et al., 2024). Thus, the primary application areas of the research findings encompassed urban areas characterized by tropical and temperate monsoon climates, as well as Mediterranean climate regions resembling the study's experimental area. This is one of the main limitations of this study.

On the other hand, the original intent of the study was to systematically interpret the spatial correlations between urban morphology and temporal variations in thermal anomaly events using rich urban morphology information contained within remote sensing images and interpretable machine learning techniques. However, due to limitations in the coverage of data provided by the Yale Center for Earth Observation (Version 5) dataset, the study was confined to discussing the relationship between the characteristic changes in urban thermal anomaly events during two seasons (summer and winter) and two time periods (day and night) with urban morphology. Consequently, the study fell short in thoroughly deciphering the mechanisms behind the formation of multi-time period, annual urban thermal anomaly events. This limitation represented a primary drawback of the study and underscored a significant area for future improvements.

5. Conclusions

With the assistance of CNNs and interpretable machine learning algorithms, this study proficiently identifies the morphological indicators linked to urban thermal anomalies. Furthermore, it delineates the nonlinear trends, thresholds, and activation levels of these indicators, elucidating their influence on the location, timing, and seasonal occurrence of thermal anomalies. The key findings are summarized as follows:

1. A ResNet-18-PTF-AFC model for urban thermal anomalies simulation using remote sensing imagery slices was constructed. The final optimized model achieved notable results with an accuracy of 79.52 % on the training set and 80.42 % on the test set. Incorporating 500 m-scale remote sensing images enhanced the model's predictive capabilities, highlighting the efficacy of the proposed methodology.
2. Grad-CAM's identification of pivotal hotspot pixels and SHAP's interpretability assessment for ResNet-18-PTF-AFC model highlighted that crucial urban morphology factors contributing to thermal anomalies include the area of green spaces, water spaces, the number of residential facilities, building floor area ratio, and the count of industrial production facilities.
3. Clear nonlinear relationships were observed between dominant urban morphology factors and the occurrence of thermal anomalies, revealing multiple thresholds and activation levels. Green Space Area (GS) affects Urban Cold Islands (UCI) and Urban Heat Islands (UHI) differently, with UCI increasing until 90 m^2 and UHI decreasing until 9 m^2. The number of living and residential facilities (LIF) impacts UHI dynamics around 68–70 and peaks at 130–147. Building floor area ratio (BD) affects UHI until 1.1 and UCI until 1.3. Road density (RD) shows a UCI threshold at 1.2. Industrial production facilities (PRO) display UHI thresholds at 16 and 44. Water space area (WS) decreases UHI until 69 m^2 and increases UCI until 106 m^2. The number of social welfare facilities (SOC) lacks significant nonlinear relationships with specific thermal anomalies. These findings offer insights into complex urban dynamics and thermal variations.

The above exploration of the nonlinear correlation between urban morphology and thermal anomalies serves to enrich theoretical insights within the fields of urban planning and environmental thermal dynamics. Moreover, it provides a quantitative framework essential for devising sustainable urban planning strategies geared towards alleviating thermal anomalies. Through the delineation of distinct types, thresholds, and activation levels of crucial urban morphology indicators correlated with thermal anomalies, this research aids in establishing precise benchmarks for urban morphology, thereby facilitating targeted mitigation measures.

CRediT authorship contribution statement

Jingxuan Hu: Writing – original draft, Software. **Tianhui Fan:** Conceptualization. **Xiaolan Tang:** Funding acquisition. **Zhijie Yang:** Software. **Yujie Ren:** Writing – review & editing, Writing – original draft, Funding acquisition, Formal analysis, Data curation, Conceptualization.

Declaration of competing interest

The authors declare that they have no known competing financial interests or personal relationships that could have appeared to influence the work reported in this paper.

Data availability

The datasets generated or analyzed during this study are available from the corresponding author on reasonable request.

Acknowledgments

This research was funded by Humanities and Social Sciences Fund of the Ministry of Education, grant number 23YJCZH177 and 22YJA760075; Undergraduate Practical Innovation Training Program Project, grant number 202310298048Z; and JST, the establishment of university fellowships towards the creation of science technology innovation, grant number JPMJFS2132.

Appendix 1:. Raw data

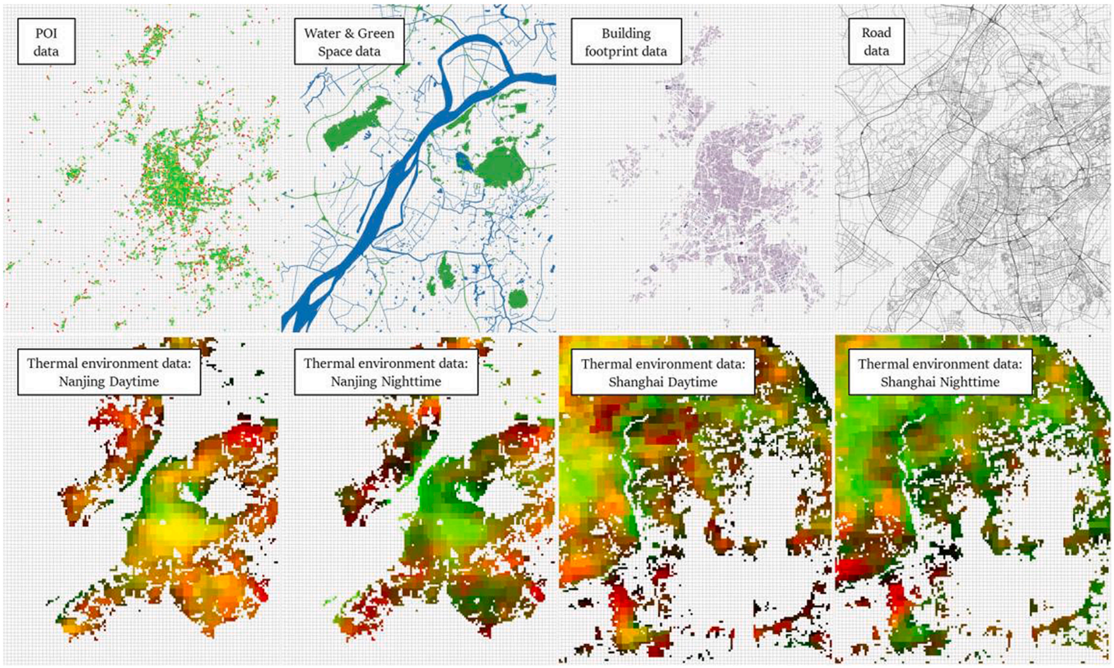

References

Abitbol, J.L., Karsai, M. Socioeconomic correlations of urban patterns inferred from aerial images: interpreting activation maps of Convolutional Neural Networks. arXiv, Apr. 10, 2020. Accessed: Sep. 05, 2023. [Online]. Available: http://arxiv.org/abs/2004.04907.

Benhammou, Y., et al., "Sentinel2GlobalLULC: A Sentinel-2 RGB image tile dataset for global land use/cover mapping with deep learning," Sci Data, vol. 9, no. 1, Art. no. 1, Nov. 2022, doi: 10.1038/s41597-022-01775-8.

Boukhabla, M., Alkama, D., Bouchair, A., 2013. The effect of urban morphology on urban heat island in the city of Biskra in Algeria. Int. J. Ambient Energy 34 (2), 100–110. https://doi.org/10.1080/01430750.2012.740424.

Chakraborty, T., Lee, X., 2019. A simplified urban-extent algorithm to characterize surface urban heat islands on a global scale and examine vegetation control on their spatiotemporal variability. Int. J. Appl. Earth Obs. Geoinf. 74, 269–280. https://doi.org/10.1016/j.jag.2018.09.015.

Chen, S., He, P., Yu, B., Wei, D., Yang, C., 2024. The challenge of noise pollution in high-density urban areas: relationship between 2D/3D urban morphology and noise perception. Build. Environ., 111313 https://doi.org/10.1016/j.buildenv.2024.111313.

Chen, A., Yao, X.A., Sun, R., Chen, L., 2014. Effect of urban green patterns on surface urban cool islands and its seasonal variations. Urban For. Urban Green. 13 (4), 646–654. https://doi.org/10.1016/j.ufug.2014.07.006.

Chun, B., Guldmann, J.-M., 2014. Spatial statistical analysis and simulation of the urban heat island in high-density central cities. Landsc. Urban Plan. 125, 76–88. https://doi.org/10.1016/j.landurbplan.2014.01.016.

Emmanuel, R., Fernando, H.J.S., 2007. Urban heat islands in humid and arid climates: role of urban morphology and thermal properties in Colombo, Sri Lanka and Phoenix, USA. Climate Res. 34 (3), 241–251. https://doi.org/10.3354/cr00694.

Eugenio Pappalardo, S., Zanetti, C., Todeschi, V., 2023. Mapping urban heat islands and heat-related risk during heat waves from a climate justice perspective: a case study in the municipality of Padua (Italy) for inclusive adaptation policies. Landsc. Urban Plan. 238, 104831 https://doi.org/10.1016/j.landurbplan.2023.104831.

Fitria, R., Kim, D., Baik, J., Choi, M., 2019. Impact of biophysical mechanisms on urban heat island associated with climate variation and urban morphology. Sci. Rep. 9 (1) https://doi.org/10.1038/s41598-019-55847-8.

Ghosh, S., Das, A., 2018. Modelling urban cooling island impact of green space and water bodies on surface urban heat island in a continuously developing urban area. Model. Earth Syst. Environ. 4 (2), 501–515. https://doi.org/10.1007/s40808-018-0456-7.

"Global Surface UHI Explorer | Center for Earth Observation." Accessed: Nov. 28, 2023. [Online]. Available: https://yceo.yale.edu/research/global-surface-uhi-explorer.

Hathway, E.A., Sharples, S., 2012. The interaction of rivers and urban morphology in mitigating the Urban Heat Island effect: a UK case study. Build. Environ. 58, 14–22. https://doi.org/10.1016/j.buildenv.2012.06.013.

Hu, L., Li, Q., 2020. Greenspace, bluespace, and their interactive influence on urban thermal environments. Environ. Res. Lett. 15 (3), 034041 https://doi.org/10.1088/1748-9326/ab6c30.

Huang, H., et al., 2019. Dynamic path planning based on improved D* algorithms of gaode map. in 2019 IEEE 3rd Information Technology, Networking Electronic and Automation Control Conference (ITNEC) 1121–1124. https://doi.org/10.1109/ITNEC.2019.8729438.

Kang, S., Lee, D., Park, J., Jung, J., 2022. Exploring urban morphologys vulnerable to urban heat islands: a multiscale analysis. Sustainability 14. https://doi.org/10.3390/su14063603.

Kotharkar, R., Bagade, A., 2018. Evaluating urban heat island in the critical local climate zones of an Indian city. Landsc. Urban Plan. 169, 92–104. https://doi.org/10.1016/j.landurbplan.2017.08.009.

Kovats, R.S., Hajat, S., 2008. Heat stress and public health: a critical review. Annu. Rev. Public Health 29 (1), 41–55. https://doi.org/10.1146/annurev.publhealth.29.020907.090843.

Lemonsu, A., Viguié, V., Daniel, M., Masson, V., 2015. Vulnerability to heat waves: Impact of urban expansion scenarios on urban heat island and heat stress in Paris (France). Urban Clim. 14, 586–605. https://doi.org/10.1016/j.uclim.2015.10.007.

Li, Y., Schubert, S., Kropp, J.P., Rybski, D. On the influence of density and morphology on the Urban Heat Island intensity, Nat Commun, vol. 11, no. 1, Art. no. 1, May 2020, doi: 10.1038/s41467-020-16461-9.

Li, X., Song, J., Lin, T., Dixon, J., Zhang, G., Ye, H., 2016. Urbanization and health in China, thinking at the national, local and individual levels. Environ. Health 15 (1), S32. https://doi.org/10.1186/s12940-016-0104-5.

Liang, Z., et al., 2021. The mediating effect of air pollution in the impacts of urban morphology on nighttime urban heat island intensity. Sustain. Cities Soc. 74, 102985 https://doi.org/10.1016/j.scs.2021.102985.

Liu, H., Huang, B., Zhan, Q., Gao, S., Li, R., Fan, Z., 2021. The influence of urban morphology on surface urban heat island and its planning implications: evidence from 1288 urban clusters in China. Sustain. Cities Soc. 71, 102987 https://doi.org/10.1016/j.scs.2021.102987.

Liu, Y., Li, Q., Yang, L., Mu, K., Zhang, M., Liu, J., 2020. Urban heat island effects of various urban morphologies under regional climate conditions. Sci. Total Environ. 743, 140589 https://doi.org/10.1016/j.scitotenv.2020.140589.

Liu, X., Ming, Y., Liu, Y., Yue, W., Han, G., 2022. Influences of landform and urban morphology factors on urban heat island: comparative case study between chengdu and chongqing. Sci. Total Environ. 820, 153395 https://doi.org/10.1016/j.scitotenv.2022.153395.

Liu, N., Morawska, L., 2020. Modeling the urban heat island mitigation effect of cool coatings in realistic urban morphology. J. Clean. Prod. 264, 121560 https://doi.org/10.1016/j.jclepro.2020.121560.

Loughner, C.P., Allen, D.J., Zhang, D.-L., Pickering, K.E., Dickerson, R.R., Landry, L., 2012. Roles of urban tree canopy and buildings in urban heat island effects: parameterization and preliminary results. J. Appl. Meteorol. Climatol. 51 (10), 1775–1793. https://doi.org/10.1175/JAMC-D-11-0228.1.

Lu, X., Lange, E., 2024. Examining the effectiveness of urban planning exhibitions in planning communication: a contextual model of learning. Cities 147, 104830. https://doi.org/10.1016/j.cities.2024.104830.
Meng, M., Xi, C., Zhuangbo, F., Cao, S.-J., 2022. Environmental co-benefits of urban design to mitigate urban heat island and PM 2.5 pollution: considering prevailing wind's effects. Indoor and Built Environment. https://doi.org/10.1177/1420326X221076815.
Mete, M.O., Yomralioglu, T., 2021. Implementation of serverless cloud GIS platform for land valuation. Int. J. Digital Earth 14 (7), 836–850. https://doi.org/10.1080/17538947.2021.1889056.
Nuruzzaman, M., 2015. Urban heat island: causes, effects and mitigation measures -a review. International Journal of Environmental Monitoring and Analysis 3, 67–73. https://doi.org/10.11648/j.ijema.20150302.15.
O'Shea, K., Nash, R. An Introduction to Convolutional Neural Networks, arXiv.org. Accessed: Nov. 28, 2023. [Online]. Available: https://arxiv.org/abs/1511.08458v2.
Ojima, T., 1990. Changing Tokyo Metropolitan area and its heat island model. Energ. Buildings 15 (1), 191–203. https://doi.org/10.1016/0378-7788(90)90131-2.
Oliveira, A., Lopes, A., Soares, A., 2022. Excess heat factor climatology, trends, and exposure across european functional urban areas. Weather Clim. Extremes 36, 100455. https://doi.org/10.1016/j.wace.2022.100455.
Parsa, A.B., et al., 2020. Toward safer highways, application of XGBoost and SHAP for real-time accident detection and feature analysis. Accid. Anal. Prev. 136, 105405.
Peng, W., Wang, R., Duan, J., Gao, W., Fan, Z., 2022. Surface and canopy urban heat islands: does urban morphology result in the spatiotemporal differences? Urban Clim. 42, 101136 https://doi.org/10.1016/j.uclim.2022.101136.
Qi, L., Lu, X., Li, X., 2019. Exploiting spatial relation for fine-grained image classification. Pattern Recogn. 91, 47–55. https://doi.org/10.1016/j.patcog.2019.02.007.
Qiang, C., Leydon, J., He, Y., 2023. Impact of COVID-19 restrictions on the urban thermal environment of Edmonton, Canada. Environ. Manag. 72 (4), 862–882. https://doi.org/10.1007/s00267-023-01813-0.
Ramírez-Aguilar, E.A., Lucas Souza, L.C. Urban morphology and population density: Influences on Urban Heat Island intensities in Bogotá, Colombia, Urban Climate, vol. 29, p. 100497, Sep. 2019, doi: 10.1016/j.uclim.2019.100497.
Rizwan, A.M., Dennis, L.Y.C., Liu, C., 2008. A review on the generation, determination and mitigation of Urban Heat Island. J. Environ. Sci. 20 (1), 120–128. https://doi.org/10.1016/S1001-0742(08)60019-4.
Sanagar Darbani, E., Monsefi Parapari, D., Boland, J., Sharifi, E., 2021. Impacts of urban morphology and urban heat island on the outdoor thermal comfort: a pilot study on Mashhad. Int. J. Biometeorol. 65 (7), 1101–1117. https://doi.org/10.1007/s00484-021-02091-3.
Santamouris, M., Synnefa, A., Karlessi, T., 2011. Using advanced cool materials in the urban built environment to mitigate heat islands and improve thermal comfort conditions. Sol. Energy 85 (12), 3085–3102. https://doi.org/10.1016/j.solener.2010.12.023.
Schwarz, N., Manceur, A.M., 2015. Analyzing the influence of urban morphologys on surface urban heat islands in Europe. J. Urban Plann. Dev. 141 (3), A4014003. https://doi.org/10.1061/(ASCE)UP.1943-5444.0000263.
Selvaraju, R.R., Cogswell, M., Das, A., Vedantam, R., Parikh, D., Batra, D. Grad-CAM: visual explanations from deep networks via gradient-based localization.
Sharma, R., Pradhan, L., Kumari, M., Bhattacharya, P., 2021. Assessing urban heat islands and thermal comfort in Noida City using geospatial technology. Urban Clim. 35, 100751 https://doi.org/10.1016/j.uclim.2020.100751.
Steeneveld, G.J., Koopmans, S., Heusinkveld, B.G., van Hove, B., Holtslag, A.A.M., 2011. Quantifying urban heat island effects and human comfort for cities of variable size and urban morphology in the Netherlands. JGR Atmospheres 116, D20129. https://doi.org/10.1029/2011JD015988.
Stone, B., Rodgers, M.O., 2001. Urban morphology and thermal efficiency: how the design of cities influences the urban heat island effect. J. Am. Plann. Assoc. 67 (2), 186–198. https://doi.org/10.1080/01944360108976228.
Targ, S., Almeida, D., Lyman, K. Resnet in resnet: generalizing residual architectures, arXiv.org. Accessed: Nov. 28, 2023. [Online]. Available: https://arxiv.org/abs/1603.08029v1.
Terjung, W.H., Louie, S.-S.-F., 1973. Solar radiation and urban heat islands. Ann. Assoc. Am. Geogr. 63 (2), 181–207. https://doi.org/10.1111/j.1467-8306.1973.tb00918.x.
Tremeac, B., et al., 2012. Influence of air conditioning management on heat island in Paris air street temperatures. Appl. Energy 95, 102–110. https://doi.org/10.1016/j.apenergy.2012.02.015.
Twardosz, R., Kossowska-Cezak, U., 2021. Large-area thermal anomalies in Europe (1951–2018). Temporal and spatial patterns. Atmos. Res. 251, 105434 https://doi.org/10.1016/j.atmosres.2020.105434.
Vargas-Munoz, J.E., Srivastava, S., Tuia, D., Falcão, A.X., 2021. OpenStreetMap: challenges and opportunities in machine learning and remote sensing. IEEE Geosci. Remote Sens. Mag. 9 (1), 184–199. https://doi.org/10.1109/MGRS.2020.2994107.
Watkins, R., Palmer, J., Kolokotroni, M., 2023. Increased temperature and intensification of the urban heat island: implications for human comfort and urban design. Accessed.
Xing, X., et al., 2020. Mapping human activity volumes through remote sensing imagery. IEEE J. Sel. Top. Appl. Earth Observations Remote Sensing 13, 5652–5668. https://doi.org/10.1109/JSTARS.2020.3023730.
Yang, Z., Luo, T., Wang, D., Hu, Z., Gao, J., Wang, L. Learning to Navigate for Fine-grained Classification, presented at the Proceedings of the European Conference on Computer Vision (ECCV), 2018, pp. 420–435. Accessed: Nov. 28, 2023. [Online]. Available: https://openaccess.thecvf.com/content_ECCV_2018/html/Ze_Yang_Learning_to_Navigate_ECCV_2018_paper.html.
Yang, F., Lau, S.S.Y., Qian, F., 2011. Urban design to lower summertime outdoor temperatures: an empirical study on high-rise housing in Shanghai. Build. Environ. 46 (3), 769–785. https://doi.org/10.1016/j.buildenv.2010.10.010.
Yang, J., Wang, Y., Xiu, C., Xiao, X., Xia, J., Cui, J., 2020. Optimizing local climate zones to mitigate urban heat island effect in human settlements. J. Clean. Prod. 275, 123767 https://doi.org/10.1016/j.jclepro.2020.123767.
Yin, S., Xiao, S., Ding, X., Fan, Y., 2024. Improvement of spatial-temporal urban heat island study based on local climate zone framework: a case study of Hangzhou, China. Build. Environ. 248, 111102 https://doi.org/10.1016/j.buildenv.2023.111102.
Yin, C., Yuan, M., Lu, Y., Huang, Y., Liu, Y., 2018. Effects of urban morphology on the urban heat island effect based on spatial regression model. Sci. Total Environ. 634, 696–704. https://doi.org/10.1016/j.scitotenv.2018.03.350.
Zhang, W., Jiang, J., Zhu, Y., 2015. Change in urban wetlands and their cold island effects in response to rapid urbanization. Chin. Geogr. Sci. 25 (4), 462–471. https://doi.org/10.1007/s11769-015-0764-z.
Zhao, W., Du, S., 2016. Learning multiscale and deep representations for classifying remotely sensed imagery. ISPRS J. Photogramm. Remote Sens. 113, 155–165. https://doi.org/10.1016/j.isprsjprs.2016.01.004.
Zhou, B., Rybski, D., Kropp, J.P., 2017. The role of city size and urban morphology in the surface urban heat island. Sci. Rep. 71 (1) https://doi.org/10.1038/s41598-017-04242-2.
Zhu, X.X., et al., 2017. Deep learning in remote sensing: a comprehensive review and list of resources. IEEE Geoscience and Remote Sensing Magazine 5 (4), 8–36. https://doi.org/10.1109/MGRS.2017.2762307.
Zurowietz, M., Langenkämper, D., Hosking, B., Ruhl, H.A., Nattkemper, T.W., 2018. MAIA—a machine learning assisted image annotation method for environmental monitoring and exploration. PLoS One 13 (11), e0207498.